

Lightweight Neural Framework for Robust 3D Volume and Surface Estimation from Multi-View Images

Diego E. Farchione Ramzi Idoughi Peter Wonka

KAUST, Saudi Arabia

{diegoeustachio.farchione, ramzi.idoughi, peter.wonka}@kaust.edu.sa

Abstract

Accurate estimation of object volume and surface area from visual data is an open challenge with broad implications across various domains. We propose a unified framework that predicts volumetric and surface metrics directly from a set of 2D multi-view images. Our approach first generates a point cloud from the captured multi-view images using recent 3D reconstruction techniques, while a parallel 2D encoder aggregates view-aligned features. A fusion module then aligns and merges 3D geometry with 2D visual embeddings, followed by a graph-based decoder that regresses volume, surface area, and their corresponding uncertainties. This proposed architecture maintains robustness against sparse or noisy data. We evaluate the framework across multiple application domains: corals, where precise geometric measurements support growth monitoring; food items, where volume prediction relates to dietary tracking and portion analysis; and human bodies, where volumetric cues are crucial for anthropometric and medical applications. Experimental results demonstrate the reliable performance of our framework across diverse scenarios, highlighting its versatility and adaptability. Furthermore, by coupling 3D reconstruction with neural regression and 2D features, our model provides a scalable and fast solution for quantitative shape analysis from visual data.

1. Introduction

Estimating the volume and surface area of objects from visual data is a critical task with profound implications across a wide range of domains. These measurements enable different applications, such as coral growth monitoring, which is a key element in reef conservation efforts, personalized dietary planning, and anthropometry for medical diagnostics. Yet, this task remains challenging due to the inherent complexities of deriving accurate 3D properties from 2D images. Conventional techniques typically rely on manual measurements or 3D reconstruction workflows, which

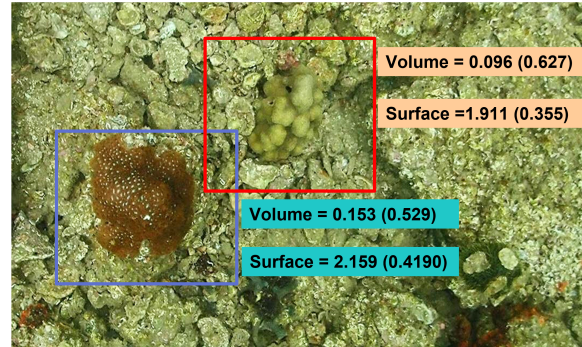


Figure 1. **Teaser:** Our end-to-end pipeline for robust volume and surface area estimation from multi-view images is demonstrated on corals from the CoralVOS dataset [48]: Using only five top-view RGB images from monocular video, our model can predict normalized volume and surface with their corresponding confidence, showcasing its potential for efficient, real-world applications.

generate a mesh from multi-view images and subsequently calculate volume and surface area using established geometric algorithms. For coral-related applications, for example, these conventional techniques [9, 45] exhibit notable shortcomings, including the need for sophisticated scanning equipment, substantial human oversight, and extensive post-processing requirements. Consequently, these approaches lack scalability, hindering their effectiveness in large-scale environmental monitoring efforts. These limitations are echoed in other domains, where factors like sparse viewpoints, the requirement to obtain a watertight mesh, inaccurate calibration, and reconstruction artifacts often degrade the quality of the derived measurements, while full geometric post-processing adds substantial latency.

In recent years, the evolution of deep learning has transformed visual data processing, offering promising avenues for overcoming these challenges. On one hand, General-purpose 3D reconstruction systems like the Visual Geometry Grounded Transformer (VGGT) [41] and MapAnything [15] enable rapid point cloud generation from

multi-view inputs with far less hand-tuning than classical pipelines. Meanwhile, point-cloud networks—including PointNet/PointNet++ [30, 31], DGCNN [42], PointTransformer [47], GCN [17], GIN [43], and related variants—excel at learning directly from unordered sets with locality and invariance priors. On the other hand, state-of-the-art 2D encoders such as DINOv3 [38] provide robust feature extraction from images. Together, these developments facilitate end-to-end frameworks that integrate multi-modal information—combining the strengths of 2D visual cues with 3D structural insights—for more efficient quantitative metric predictions. However, most existing systems still focus on intermediate tasks like geometry reconstruction or image synthesis, relegating volume and surface estimation to post-processing, which limits their practicality and generalizability across diverse scenarios.

To address these gaps, we propose a *Lightweight Neural Framework for Robust 3D Volume and Surface Estimation from Multi-View Images*. This end-to-end approach begins by masking the object of interest using advanced promptable segmentation tools for precise isolation. Next, it applies general-purpose multi-view reconstructors, such as MapAnything or VGGT, to generate a detailed point cloud from the processed views. A compact point-cloud network then serves as an encoder to derive a latent vector from this representation. Simultaneously, features are extracted from the 2D images using a state-of-the-art encoder like DINOv3, which are merged with the 3D latent vector. Finally, a Fully Connected (FC) network acts as the decoder to estimate volume and surface metrics along with their confidence levels, achieved through two parallel branches that employ specialized encoder-decoder networks for each metric. Trained with a composite loss for uncertainty-aware predictions, our framework ensures efficient and scalable results across diverse domains, while eliminating the need for heavy mesh processing and maintaining robustness to sparse or noisy data.

The key contributions of our approach are as follows:

- **Streamlined end-to-end metrics regression.** A lightweight framework that directly predicts volume and surface area from masked multi-view inputs, bypassing traditional mesh generation and post-processing for greater efficiency. Thus, our framework supports efficient deployment across large-scale applications without compromising performance.
- **Integrated 2D-3D feature fusion.** By combining advanced 2D feature extraction with compact point-cloud encoding and parallel prediction branches, our method enhances robustness to challenges like sparse views and noise.
- **Uncertainty-aware predictions.** Our framework incorporates a composite training objective to provide calibrated confidence estimates for volume and surface mea-

surements, enhancing reliability specifically for scientific applications.

- **Extensive evaluation on synthetic and real-world data.**

Through comprehensive assessments on both synthetic and real datasets, we showcase superior accuracy, robustness, particularly in handling imperfect data scenarios, and effective generalization to various fields, such as coral monitoring, dietary planning, and anthropometry.

2. Related Work

2.1. 3D Reconstruction from Multi-View Images

Traditional multi-view stereo (MVS) pipelines, such as those based on Structure from Motion (SfM) and dense reconstruction (e.g., COLMAP [36] or PMVS [7]), rely on photometric consistency and keypoint matching (e.g., SIFT [25]) to generate point clouds or meshes. While effective, these methods often require dense views, accurate calibration, and extensive post-processing, making them computationally intensive and prone to failures in textureless or sparse-view scenarios.

Recent neural approaches have improved efficiency and robustness. Methods like NeRF [27] and its variants (e.g., Mip-NeRF [3], Instant-NGP [28]) enable implicit 3D scene reconstruction from multi-view images, while explicit techniques like 3D Gaussian Splatting [16] accelerate rendering. Generalizable models, such as VGGT [41] and MapAnything [15], extend this to sparse inputs by learning view-invariant features. However, these systems typically focus on geometry recovery and require separate post-processing for volume and surface area estimation, limiting their applicability in real-time or noisy settings. Our framework leverages these advancements (e.g., point cloud generation) but extends them by integrating 2D features and directly regressing metrics, thereby avoiding the need for heavy mesh-based workflows.

2.2. Volume Estimation in Specific Domains

In domain-specific applications, volume estimation has been explored extensively. For food items, early methods used multi-view stereo [5] or RGB-D sensors [8, 37] to reconstruct 3D models of the food for dietary analysis. Other works leverage single RGB images by requiring a fiducial marker or reference object (such as a coin or a specific plate size) to resolve scale ambiguity [6, 14, 29, 39, 46]. Recent deep learning approaches, such as VolEta [1] and Vol-Tex [2], directly regress volume from images. These works improve scalability for portion tracking but often assume controlled environments like the presence of a checkerboard pattern [40] and struggle with sparse views or occlusions, as seen in real-world dietary apps. In a similar manner, estimating the volume of human bodies and their parts plays a vital role in monitoring health metrics such as obesity, mus-

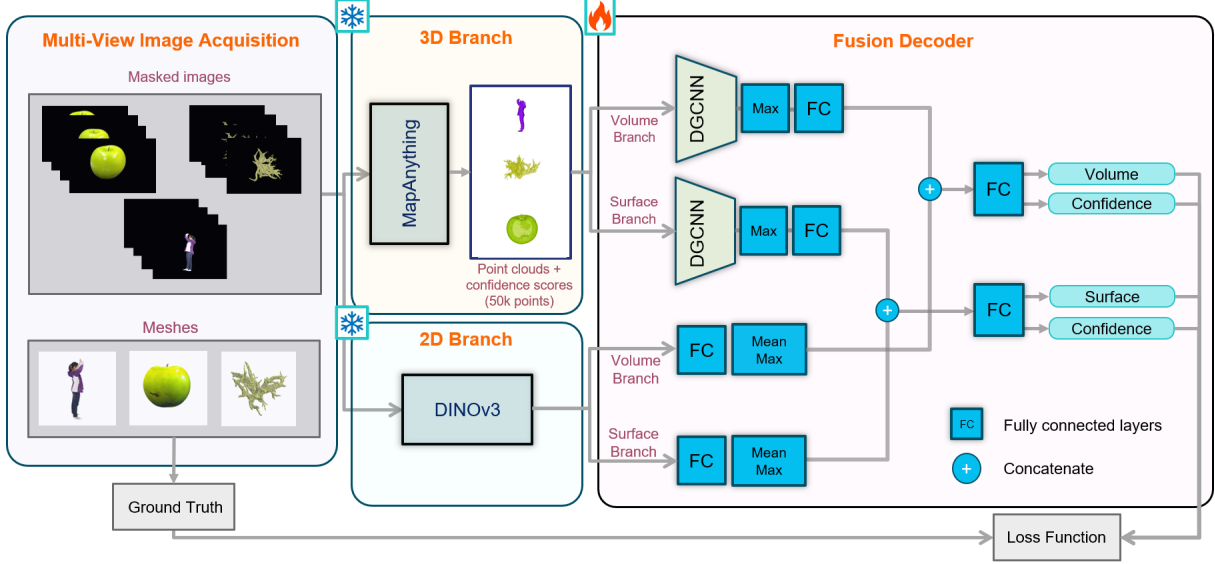


Figure 2. From masked multi-view images from meshes (or original images), a 3D reconstructor like MapAnything produces a fused point cloud with per-point confidence, while a frozen DINOv3 encoder extracts view-aligned 2D features. In the fusion decoder, a lightweight DGCNN summarizes the point cloud, followed by max pooling layer. In the 2D branch, per-view features pass through a small FC block and are mean-max pooled across views. The fusion decoder concatenates the 3D and 2D descriptors for each target and feeds a small FC regressor that outputs Volume and Surface along with their Confidence (log-variance). A composite loss (Gaussian NLL in linear/log domains + MAPE) trains the heads end-to-end, yielding single-pass volume/surface estimates without the need to reconstruct watertight meshes or applying heavy post-processing.

cle atrophy, and lymphedema. Traditional methods employ structured light or RGB-D sensors (e.g., Kinect) to capture full-body 3D scans, from which meshes are derived for volume computation. However, these techniques often require subjects to remain motionless for extended durations, rendering them unsuitable for certain populations, like elderly and bedridden patients. To address this limitation, Lunscher and Zelek [26] leveraged convolutional neural networks to predict the opposite-view depth image from a single input depth image. Their proposed 3D reconstruction is obtained by combining the 3D points from both images. However, this requires additional postprocessing steps (e.g., denoising, surface completion), which introduce new errors and depend on complementary techniques for accurate volume estimation. More recently, deep learning models like VolNet [22] exploit intermediate 2D and 3D pose estimations along with body part segmentation from a single RGB image to regress part-specific volumes, while approaches such as Point2PartVolume [10] utilize a single depth image to predict clothed, part-aware body shapes and compute volumes accordingly. These methods commonly draw on parametric body models, like SMPL [24], to enforce plausible human shapes. For coral monitoring, existing pipelines [9, 19, 21, 45] rely on SfM or tomography scanning to assess growth, which requires high-fidelity inputs and substantial manual oversight. This reliance on precise,

dense data hinders large-scale deployment, particularly in challenging environmental conditions where sparse or variable imagery is common.

Across these domains, persistent limitations, such as the need for controlled setups, extensive postprocessing, and vulnerability to data imperfections, underscore the demand for more robust, end-to-end solutions.

3. Methods

3.1. Overview

Our pipeline architecture, as shown in Figure 2, takes as input a set of multi-view RGB images of a single object and is trained to output both the volume and surface area, along with their associated confidence. It consists of four main components: (1) This pre-processing step segments the target object to generate masked multi-view images, isolating the object from its background. This segmentation step is performed using Grounded-SAM2, which combines Grounding DINO and SAM 2 for promptable, open-world segmentation [13, 18, 23, 33–35]. (2) **3D Branch:** This component recovers and fuses per-view geometry from the masked images into a unified point cloud with associated confidences, which serves as the geometric backbone after a simple normalization. (3) **2D Branch:** The third component extracts DINOv3 features from the masked views. These components are based on foundational models, which

are not fine-tuned as part of our pipeline. (4) **Fusion decoder:** In this final step, two parallel architectures independently regress the volume and surface area. Each architecture employs a DGCNN-style network augmented with a shallow fully connected layer to encode the 3D point cloud into a latent code; on the 2D side, a shallow fully connected network with a pooling layer encodes the multi-view DINOv3 features into a compact global descriptor. Regression is then performed by an FC-based decoding head on the concatenated latent code and global descriptor. Uncertainties are also predicted using an uncertainty-aware loss. In the following, we describe each component of our framework in detail.

3.2. Features Extraction

To enable accurate estimation of volume and surface area for 3D objects, we combine complementary 2D and 3D representations derived from sparse multi-view inputs. Indeed, the 3D representation (e.g., point cloud) captures essential geometric shape and spatial dimensions, while the 2D image conveys visual details like textures and edges. This integration ensures a more robust understanding by leveraging both modalities, preventing the limitations of relying on either alone.

2D Feature Extraction: We utilize a DINOv3 ViT-S/16 encoder (with a patch size of 16 and hidden/pooler dimensionality of 384) to process each masked RGB view and generate embedded features. This approach extracts global, view-aggregated descriptors that highlight visual characteristics. The feature extraction can be formulated as follows:

$$d_{2D}^k = f^{DINO}(I_k) \quad k = 1..N \quad (1)$$

where: d_{2D}^k is the feature vector extracted using the DINOv3 architecture $f^{DINO}(\cdot)$, from the k^{th} masked image $I_k \in \mathbb{R}^{3 \times H \times W}$.

3D Feature Extraction: For the 3D representation, we employ a general-purpose multi-view reconstruction model to produce a sparse, fused point cloud with per-point confidence scores. In our primary setup, we leverage the MapAnything framework with optimized settings for efficiency, applied to masked inputs. The model outputs 3D points and confidence values per view, which we aggregate across views and augment with confidence as an additional channel, resulting in features of the form $(x, y, z, conf)$. We post-process this feature vector using two filters: a mask-aware gate to remove points linked to background pixels and a background-suppression mechanism to eliminate low-confidence artifacts, ensuring a cleaner point cloud. To optimize memory usage, we subsample the points to a maximum of 50,000 per object, using random selection for data augmentation during training and prioritizing higher-confidence points during inference. This process is ex-

pressed as:

$$d_{3D} = f^P(I) = (x, y, z, conf)_{[0:50k]} \quad (2)$$

where: $d_{3D} \in \mathbb{R}^{4 \times 50k}$ is the extracted feature vector, f^P is the multi-view reconstruction pipeline (MapAnything in our primary setup or VGPT), $I = (I_k)_k$ is the set of N masked images.

3.3. Feature Fusion and Regression

In the final module of our pipeline, we employ two parallel and independent branches for estimating volume and surface area, respectively, which share the same architecture but are trained separately for specialized outputs. This module fuses complementary 2D and 3D features to create a unified representation, enabling accurate estimation of the object's properties. The 3D features, derived from the point cloud, are processed through a graph-based network, following a DGCNN architecture, that aggregates point-wise information into a compact embedding, ensuring permutation invariance, which is further refined using max pooling and a multi-layer perceptron (MLP) to produce the final 3D latent code, denoted as: z_{3D} . Meanwhile, the 2D features from multiple views are aggregated into a single global descriptor d_{2D} , achieved by passing each view's features through a shallow MLP and then combining them via mean and max pooling across views. At this stage, we concatenate the 2D and 3D representation features $[z_{3D} \parallel d_{2D}]$ and feed it to a last FC network that acts as the regression head and outputs (i) a positive volume (or surface) enforced by the use of a softplus activation. (ii) a raw log σ^2 used in a Gaussian Negative Log-Likelihood (NLL) for calibrated aleatoric uncertainty. Additional implementation details are available in the supplement.

4. Training

4.1. Datasets Preparation

In our training pipeline, we first train a coarse version of the model on the Objaverse dataset for robust generalization, followed by fine-tuning on domain-specific datasets (**Synthetic Corals**, **THuman2.1** [44], and **MetaFood** [4]) to adapt to particular applications. In Figure 3, we illustrate some assets from each of these datasets. This approach leverages Objaverse for initial broad learning and subsequent specialization for accurate volume and surface area estimation. Another motivation for this training approach is the lack of large datasets in the specific applications.

For the Objaverse dataset, we select meshes and process them with ManifoldPlus [12] to ensure they are watertight, enabling reliable geometry. We then generate multi-view images through projections and compute ground-truth (GT) volume and surface area metrics from these watertight



Figure 3. **Representative samples across datasets.** Top: food items from the *MetaFood* dataset. Middle: human subjects from *THuman2.1*. Bottom: synthetic coral specimens generated with *Infinigen* and *ManifoldPlus*. These examples highlight the geometric and visual diversity of the domains on which our framework performs unified volume and surface estimation.

meshes (as explained in the following), providing a strong foundation for the initial coarse training.

Synthetic Corals: Due to the lack of adequate 3D captured Coral dataset, we constructed our own dataset of textured coral meshes generated with *Infinigen* [32] and made watertight using *ManifoldPlus*. The dataset contains more than 4000 different assets, representing corals of different species, shape and size. It will be made publicly available upon acceptance of our work.

THuman2.1: Originally this dataset contains textured human meshes, that we use to evaluate the GT metrics. We apply a similar strategy of rendering masked multi-view images with black backgrounds on roughly 2500 assets and random view sampling as for the corals

MetaFood: This dataset is composed of real food photographs. We used segmented version of these images using Grounded SAM 2, prompted by the food class name. We perform manual quality assurance to retain accurate masks, correcting inconsistencies (e.g., varying inclusion of containers) to ensure alignment with ground-truth metrics before using them in training. The final dataset size consists of 360 assets.

4.2. Data Augmentation

To enhance model robustness and generalization, we apply data augmentation techniques to the datasets during training. This includes random rigid transforms per sample, such as 3D rotations based on independent uniform angles across Euler axes and axis reflections with a 50% probability along each coordinate. These transformations are limited to the (x, y, z) coordinates of the feature vector d_{3D} , the confidence scores are left unchanged. Additionally, for datasets with variable point cloud quality, we optionally introduce a small coordinate jitter to simulate noise. For both the training and validation sets, images were randomly selected. In Sec. 5.1, we further consider randomly sampled image subsets with varying numbers of views per object.

At evaluation time, these augmentations are disabled to maintain consistency and ensure reliable, deterministic performance metrics. Further details are provided in the supplementary materials.

4.3. Loss Function

We train a single-head regressor that outputs a positive mean $\hat{y} > 0$ and the uncertainty $\widehat{\log \sigma^2}$ for each target (volume or surface). We adopt a *hybrid* loss that combines probabilistic and deterministic components. On the probabilistic side—following the Gaussian NLL formulation of Lakshminarayanan et al. [20] we assume $y \sim \mathcal{N}(\mu, \sigma^2)$ with mean $\mu = \hat{y}$ and a learned variance σ^2 . The NLL *linear* term can be expressed as follows:

$$\text{NLL}_{\text{lin}}(y, \mu, \sigma^2) = \frac{1}{2} \left(\log \sigma^2 + \frac{(y - \mu)^2}{\sigma^2} \right), \quad (3)$$

To handle the wide dynamic range of targets, we incorporate a *logarithmic* Gaussian NLL term, by computing the NLL term on logarithmically scaled data. The combined NLL loss is then weighted as:

$$\mathcal{L}_{\text{NLL}} = w_{\text{lin}} \text{NLL}_{\text{lin}} + w_{\log} \text{NLL}_{\log}, \quad (4)$$

where: w_{lin} and w_{\log} are weights such that $w_{\text{lin}} + w_{\log} = 1$

The deterministic term is the Mean Absolute Percentage Error (MAPE), which is scale-invariant, and treats over and under-estimation symmetrically in magnitude. To prevent inflation from small targets, we include a small stabilization constant ε :

$$\mathcal{L}_{\text{det}} = \frac{1}{B} \sum_{i=1}^B \frac{|\hat{y}_i - y_i|}{y_i + \varepsilon} . \quad (5)$$

Finally, the overall loss is a convex combination of these components, balancing probabilistic and deterministic aspects:

$$\mathcal{L}_{\text{tot}} = \gamma \mathcal{L}_{\text{NLL}} + (1 - \gamma) \mathcal{L}_{\text{det}}. \quad (6)$$

where: $\gamma \in \{0, 1\}$ controls the trade-off. This hybrid design ensures calibrated predictions with uncertainty awareness.

Table 1. Ablation study comparing the effects of DINOv3 features and backbone choices (VG GT vs. MapAnything) on mean and median MAPE for volume and surface reconstruction across the **Meta Food**, **THuman**, and **Synthetic Corals** datasets, using 30 images per asset.

Model	Variant	Meta Food Dataset				THuman				Synthetic Corals			
		Vol. MAPE ↓		Surf. MAPE ↓		Vol. MAPE ↓		Surf. MAPE ↓		Vol. MAPE ↓		Surf. MAPE ↓	
		mean	med.	mean	med.	mean	med.	mean	med.	mean	med.	mean	med.
VG GT	with DINO v3	64.63	39.79	21.02	14.28	5.97	4.66	3.36	2.57	15.62	10.80	11.15	10.13
VG GT	w/o DINO v3	91.49	75.74	49.05	34.89	9.16	6.92	4.93	3.63	27.11	22.14	17.50	15.03
Mapanything	with DINO v3	69.81	35.01	22.32	12.64	5.83	4.66	3.33	2.42	16.27	12.59	11.06	7.61
Mapanything	w/o DINO v3	94.21	75.48	47.81	29.10	11.62	9.73	5.71	4.41	56.87	50.92	30.86	26.72

4.4. Ground Truth Surface and Volume Estimation

In this following, we describe the methods for computing ground-truth surface area and volume metrics across our datasets, ensuring consistency and accuracy for model training and evaluation. For all data we begin with preprocessing to handle mesh quality and scaling.

For watertight preprocessing, meshes from the **Objaverse**, **THuman2.1** and **Synthetic Corals** datasets are processed using ManifoldPlus [12] to ensure watertightness, which is essential for reliable volume computations.

Normalization is applied uniformly across all datasets. For a given triangular mesh \mathcal{M} , we perform isotropic scaling such that the largest dimension of its axis-aligned bounding box is 1: $L_{\max} = \max\{\Delta x, \Delta y, \Delta z\}$, resulting in the normalized mesh $\tilde{\mathcal{M}} = \mathcal{M}/L_{\max}$. All reported metrics for MetaFood3D are based on this normalized form.

Surface area is calculated for all datasets using Trimesh, which sums the areas of individual triangles without requiring watertightness:

$$A_{GT}(\tilde{\mathcal{M}}) = \sum_{(i,j,k) \in \mathcal{F}} \frac{1}{2} \|(\mathbf{v}_j - \mathbf{v}_i) \times (\mathbf{v}_k - \mathbf{v}_i)\|, \quad (7)$$

where: \mathcal{F} represents the set of faces and $\mathbf{v}_j, \mathbf{v}_i, \mathbf{v}_k$ are the vertices of each triangle.

For volume estimation, the approach varies by dataset to account for mesh characteristics. For **Objaverse**, **THuman2.1** and **Synthetic Corals**, where meshes are watertight, we compute the signed volume using Trimesh, which sums the volumes of tetrahedra formed by each triangle and the origin. For a triangle with vertices $\mathbf{v}_{i0}, \mathbf{v}_{i1}, \mathbf{v}_{i2} \in \mathbb{R}^3$, with a counter-clockwise order when viewed from outside, the formula is provided as follows:

$$V_{\text{signed}} = \frac{1}{6} \sum_i \det[\mathbf{v}_{i0} \quad \mathbf{v}_{i1} \quad \mathbf{v}_{i2}] = \frac{1}{6} \sum_i \mathbf{v}_{i0} \cdot (\mathbf{v}_{i1} \times \mathbf{v}_{i2}). \quad (8)$$

In contrast, for **MetaFood3D**, we apply axis-aligned ray casting on the normalized mesh $\tilde{\mathcal{M}}$ to avoid distortions from watertightness repair artifacts, such as self-intersections and

over-smoothing. Rays are cast along each axis $a \in \{x, y, z\}$ on a regular grid, with interior segments identified using the even-odd rule and aggregated to estimate $\tilde{V}^{(a)}$. The final volume is the median $\tilde{V} = \text{median}\{\tilde{V}^{(x)}, \tilde{V}^{(y)}, \tilde{V}^{(z)}\}$.

This methodology ensures accurate and dataset-appropriate ground-truth metrics, supporting the evaluation and refinement of our model.

5. Results

5.1. Ablation Studies

We conducted ablation studies to analyze the contribution of the 2D branch (DINOv3) and the choice of multi-view 3D backbone (VG GT vs. MapAnything) on reconstruction performance across the **MetaFood**, **THuman**, and **Synthetic Corals** datasets. Table 1 presents the mean and median Mean Absolute Percentage Error (MAPE) for volume and surface reconstruction across the three datasets, evaluating the effects of the inclusion or exclusion of DINOv3 features and the backbone selection. Our results demonstrate that incorporating DINOv3 features significantly reduces errors for both volume and surface estimates across all datasets. Additionally, surface reconstruction consistently achieves lower MAPE values than volume reconstruction, indicating that it is inherently easier. Performance varies by dataset, with the model excelling on **THuman**, followed by **Synthetic Corals**, and then **MetaFood**. This variation can be attributed to several factors:

- The level of sample variability within each dataset;
- Potential errors in ground-truth estimation derived from meshes;
- Differences in dataset quality;
- The total number of samples available.

To provide a more comprehensive evaluation, we report both mean and median MAPE, as each offers unique insights into the error distribution. Small-volume objects amplify percentage errors for the same absolute deviation, potentially skewing the mean. For instance, while MAPE normalizes by the true value, a small absolute error of 0.3 cm^3 represents only 0.33% for a larger object like an apple of

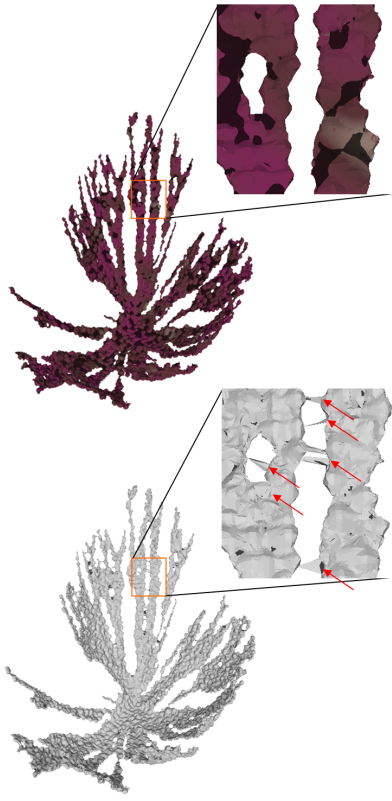


Figure 4. Watertight post-processing and low-volume sensitivity. *Top:* original reconstructed mesh. *Bottom:* watertight mesh. Enforcing watertightness introduces artifacts (spurious bridges and corrugations) and biases the volume downward on this sample. Because the object has relatively low volume, even small geometric artifacts, whether due to watertightening or ordinary reconstruction noise, can disproportionately increase per-sample MAPE, inflating the overall mean and widening the spread around the median.

90 cm³, but escalates to 33% for a tiny object like a bean of 0.9 cm³. This disproportionate effect makes the median a valuable complement for capturing central tendencies without being overly influenced by such extremes. Furthermore, factors like minor artifacts in watertight volume calculations, as illustrated in Figure 4, which shows a low-volume coral with inaccuracies in ground-truth processing, underscore the need for both metrics to account for these variabilities and ensure a balanced assessment.

Finally, Table 2 examines the model’s robustness to training with varying numbers of samples on the **THuman** dataset, showing comparable volume and surface estimation performance even with limited samples. Additional ablations are detailed in the supplementary material.

Table 2. Robustness of Volume and Surface Estimation on the **THuman Dataset: Mean and Median MAPE versus Number of Samples per Object (lower values indicate better performance).**

# Samples	Vol. MAPE ↓		Surf. MAPE ↓	
	Mean	Med.	Mean	Med.
1	12.59	10.46	7.97	5.98
2	10.76	8.04	6.83	5.47
4	10.41	7.73	6.43	4.36
8	8.88	6.40	5.44	3.94
16	8.46	6.60	5.12	3.56
32	8.13	5.60	5.00	3.21
64	8.13	5.77	5.06	3.84
100+	8.09	5.79	5.06	3.77

5.2. Comparison to Food Volume Estimation Benchmarks

We compare our method on the **MetaFood** dataset against established baselines for food volume estimation. We trained our model on subsets of **MetaFood** using $N \in \{1, 2, 4, 8, 16, 32, 64, 128, 200\}$ images per sample, employing MapAnything for reconstruction. For a fair comparison, we also evaluated a decoder variant with the NLL loss disabled (weight set to 0). We benchmarked our approach against methods like ININ and VolETA on the 20-scene protocol, as detailed in Table 3, which reports results for all samples and the hardest 5 that contain a single image. Across the 18 directly comparable scenes, our model achieved lower error on 7 out of 18 scenes, including successful reconstructions of two additional cases that prior studies omitted due to reported quality issues (see the per-scene breakdown in the supplementary material). While multi-view methods may outperform ours in scenarios with abundant views, our approach excels in the single-image setting, underscoring its robustness with sparse observations. We exclude VolTex results from this comparison, as their evaluation only covered a subsample of the protocol, making direct assessment inappropriate.

Runtime and practicality. Our model is **lightweight** and designed for deployment: it performs the forward pass in the fusion decoder in 0.72 seconds on average, and MapAnything + DINoV3 steps in inference, on average, in 27.83s for a single view 30.10s and 43.58s for 30 and 200 views respectively. Whereas, Reconstruction-based pipelines typically incur substantially higher runtimes, needing several minutes (and even 1 hour) to complete the reconstruction due to per-scene optimization or heavy rendering. Beyond speed, our architecture eliminates the need for watertight meshes or hand-crafted geometric formulas, enabling strong generalizability across datasets and flexibility with input images—from single views to many—while delivering competitive or superior accuracy on a substantial portion of the benchmark.

Table 3. MetaFood Challenge: mean and median absolute percentage errors and winning samples on the entire dataset and on single images only.

Scope	Metric	Ours	ININ	VoLETA	Trellis
All cases	Mean MAPE ↓	14.72	11.73	10.97	-
	Median MAPE ↓	8.60	9.04	6.93	-
	Winning samples ↑	9/20	4/20	7/20	-
Single-image	Mean MAPE ↓	11.91	19.16	19.12	238.20
	Median MAPE ↓	8.01	20.03	23.42	92.40
	Winning samples ↑	3/5	2/5	0/5	0/5

Table 4. Real corals and THuman: mean and median MAPE for volume and surface (lower is better). For corals, the baseline is 2DGS; for THuman, the baseline is Agisoft.

Dataset	# Views	Stat.	Ours		2DGS / Agisoft	
			Vol	Surf	Vol	Surf
Corals	20	Mean	14.23	14.89	21.30	101.89
		Median	11.33	5.96	16.75	27.97
	30	Mean	16.46	14.11	21.05	93.08
		Median	10.70	5.83	15.54	31.76
THuman	20	Mean	9.65	12.00	18.64	46.98
		Median	7.57	11.27	18.04	49.16
	30	Mean	11.79	12.62	13.45	38.12
		Median	10.39	12.18	14.42	35.85

Table 5. Real corals and THuman: mean and median MAPE for volume and surface (lower is better) for ours vs. Trellis.

Dataset	Stat.	Ours		Trellis	
		Vol	Surf	Vol	Surf
Corals	Mean	20.68	30.07	66.09	77.24
	Median	9.37	13.73	90.43	71.24
THuman	Mean	20.72	15.17	72.24	43.91
	Median	15.42	12.14	73.55	47.33

5.3. Generalization Evaluation: Comparisons with 2DGS on Real Corals and Agisoft on THuman Dataset

To evaluate our model’s real-world generalization, we tested it on a small set of real coral samples and the THuman dataset, benchmarking against 2D Gaussian Splatting [11] (2DGS), and a commercial 3D reconstruction software: Metashape Agisoft. For the corals, we collected and photographed a limited number of physical specimens, generating multi-view image sets with varying capture counts. Due to 2DGS’s reconstruction constraints, reliable results were only achievable with 20 or 30 input views, which are highlighted in Table 4.

We fine-tuned our model on this real-coral subset, starting from weights pre-trained on synthetic corals using MapAnything and DINOv3 features. Despite the limited dataset of only 11 real samples, the fine-tuned model consistently outperformed 2DGS in both mean and median er-

rors across all tested image counts. Additionally, as shown in Table 4 our framework surpassed Agisoft’s performance on a subsample of the THuman dataset. These results underscore the proposed method’s strong generalization capabilities under data scarcity, with potential for further enhancements as more annotated real samples are acquired. Examples of the collected real corals are available in the supplementary material.

5.4. Single-View Performance: Comparison with Trellis on Real Corals and THuman

We extended our evaluation to assess our framework’s performance against Trellis on the same real-coral and THuman samples in a single-view context. For each object, we processed 30 individual images, derived a volume estimate from each. The same procedure was applied to Trellis, where volume estimates were obtained directly from its reconstructed meshes using a single image generation. As detailed in Table 5, our framework surpasses Trellis across all metrics on both datasets.

6. Conclusions

We present a lightweight multi-view framework that integrates 3D point clouds with pooled DINOv3 features through a compact graph decoder, facilitating direct and efficient regression of volume and surface area. Our model achieves low mean and median MAPE across diverse domains, including foods, humans, and corals, using a single forward pass, which provides significant speed benefits over 3D reconstruction-based methods and demonstrates robustness with sparse views; even in single-image scenarios, it outperforms existing baselines. Despite these performances, limitations arise from the need for scale-normalized predictions, as training on unit-extent geometry requires an external scaling cue—such as reference objects like utensils or markers—to convert estimates to absolute measurements, though the limited availability of datasets incorporating such references poses a substantial challenge for broader adoption. Furthermore, while the model’s data efficiency is evident from its strong performance on the MetaFood dataset with only 360 samples or on real corals with few samples, opportunities for enhancement exist through the expansion of curated datasets, which could improve accuracy and strengthen cross-domain generalization by addressing gaps in representation and increasing the diversity of training examples. These limitations underscore valuable avenues for future research, positioning the framework to realize even greater precision and adaptability in practical applications.

References

- [1] Ahmad AlMughrabi, Umair Haroon, Ricardo Marques, and Petia Radeva. Voleta: One-and few-shot food volume esti-

mation. *arXiv preprint arXiv:2407.01717*, 2024.

[2] Ahmad AlMughrabi, Umair Haroon, Ricardo Marques, and Petia Radeva. Voltex: Food volume estimation using text-guided segmentation and neural surface reconstruction. In *CVPR*, pages 450–457, 2025.

[3] Jonathan T. Barron, Ben Mildenhall, Matthew Tancik, Peter Hedman, Ricardo Martin-Brualla, and Pratul P. Srinivasan. Mip-nerf: A multiscale representation for anti-aliasing neural radiance fields. In *ICCV*, 2021.

[4] Yuhao Chen, Jiangpeng He, Gautham Vinod, Siddeshwar Raghavan, Chris Czarnecki, Jinge Ma, Talha Ibn Mahmud, Bruce Coburn, Dayou Mao, Saejith Nair, et al. Metafood3d: 3d food dataset with nutrition values. *arXiv preprint arXiv:2409.01966*, 2024.

[5] Joachim Dehais, Marios Anthimopoulos, Sergey Shevchik, and Stavroula Mougiaakakou. Two-view 3d reconstruction for food volume estimation. *IEEE Transactions on Multimedia*, 19(5):1094–1104, 2017.

[6] Shaobo Fang, Fengqing Zhu, Chufan Jiang, Song Zhang, Carol J Boushey, and Edward J Delp. A comparison of food portion size estimation using geometric models and depth images. In *ICIP*, pages 26–30. IEEE, 2016.

[7] Yasutaka Furukawa and Jean Ponce. Accurate, dense, and robust multi-view stereopsis. *PAMI*, 32(8):1362–1376, 2009.

[8] Bryan Gonzalez, Gonzalo Garcia, Osmar Gecele, Jaime Ramirez, Sergio A Velastin, and Gonzalo Farias. Preliminary results on food weight estimation with RGB-D images. In *ICPRS*, pages 1–7. IEEE, 2024.

[9] Petra Helmholz, Tahlia Bassett, Liam Boyle, Nicola Browne, Iain Parnum, Molly Moustaka, and Richard Evans. Evaluating linear coral growth estimation using photogrammetry and alternative point cloud comparison methods. *The International Archives of the Photogrammetry, Remote Sensing and Spatial Information Sciences*, 48:121–128, 2024.

[10] Pengpeng Hu, Xinxin Dai, Ran Zhao, He Wang, Yingliang Ma, and Adrian Munteanu. Point2partvolume: Human body volume estimation from a single depth image. *IEEE Transactions on Instrumentation and Measurement*, 72:1–12, 2023.

[11] Binbin Huang, Zehao Yu, Anpei Chen, Andreas Geiger, and Shenghua Gao. 2D gaussian splatting for geometrically accurate radiance fields. In *ACM SIGGRAPH 2024 conference papers*, pages 1–11, 2024.

[12] Jingwei Huang, Yichao Zhou, and Leonidas Guibas. Manifoldplus: A robust and scalable watertight manifold surface generation method for triangle soups. *arXiv preprint arXiv:2005.11621*, 2020.

[13] Qing Jiang, Feng Li, Zhaoyang Zeng, Tianhe Ren, Shilong Liu, and Lei Zhang. T-rex2: Towards generic object detection via text-visual prompt synergy, 2024.

[14] Prachi Kadam, Sharnil Pandya, Shraddha Phansalkar, Mayur Sarangdhar, Nayana Petkar, Ketan Kotecha, and Deepak Garg. Fvestimator: A novel food volume estimator wellness model for calorie measurement and healthy living. *Measurement*, 198:111294, 2022.

[15] Nikhil Keetha, Norman Müller, Johannes Schönberger, Lorenzo Porzi, Yuchen Zhang, Tobias Fischer, Arno Knapitsch, Duncan Zauss, Ethan Weber, Nelson Antunes, Jonathon Luiten, Manuel Lopez-Antequera, Samuel Rota Bulò, Christian Richardt, Deva Ramanan, Sebastian Scherer, and Peter Kortschieder. Mapanything: Universal feed-forward metric 3d reconstruction, 2025.

[16] Bernhard Kerbl, Georgios Kopanas, Thomas Leimkühler, and George Drettakis. 3d gaussian splatting for real-time radiance field rendering. *TOG*, 42(4):139–1, 2023.

[17] Thomas N. Kipf and Max Welling. Semi-supervised classification with graph convolutional networks. In *ICLR*, 2017.

[18] Alexander Kirillov, Eric Mintun, Nikhila Ravi, Hanzi Mao, Chloe Rolland, Laura Gustafson, Tete Xiao, Spencer Whitehead, Alexander C. Berg, Wan-Yen Lo, Piotr Dollár, and Ross Girshick. Segment anything. *arXiv:2304.02643*, 2023.

[19] Hanna R Koch, Bailey Wallace, Allyson DeMerlis, Abigail S Clark, and Robert J Nowicki. 3D scanning as a tool to measure growth rates of live coral microfragments used for coral reef restoration. *Frontiers in Marine Science*, 8:623645, 2021.

[20] Balaji Lakshminarayanan, Alexander Pritzel, and Charles Blundell. Simple and scalable predictive uncertainty estimation using deep ensembles. *Advances in neural information processing systems*, 30, 2017.

[21] Ines D Lange and Chris T Perry. A quick, easy and non-invasive method to quantify coral growth rates using photogrammetry and 3D model comparisons. *Methods in Ecology and Evolution*, 11(6):714–726, 2020.

[22] Fabian Leinen, Vittorio Cozzolino, and Torsten Schön. Volnet: estimating human body part volumes from a single rgb image. *arXiv preprint arXiv:2107.02259*, 2021.

[23] Shilong Liu, Zhaoyang Zeng, Tianhe Ren, Feng Li, Hao Zhang, Jie Yang, Chunyuan Li, Jianwei Yang, Hang Su, Jun Zhu, et al. Grounding dino: Marrying dino with grounded pre-training for open-set object detection. *arXiv preprint arXiv:2303.05499*, 2023.

[24] Matthew Loper, Naureen Mahmood, Javier Romero, Gerard Pons-Moll, and Michael J Black. Smpl: A skinned multi-person linear model. In *Seminal Graphics Papers: Pushing the Boundaries, Volume 2*, pages 851–866. 2023.

[25] David G. Lowe. Distinctive image features from scale-invariant keypoints. *IJCV*, 60(2):91–110, 2004.

[26] Nolan Lunscher and John Zelek. Deep learning whole body point cloud scans from a single depth map. In *CVPR Workshops*, pages 1095–1102, 2018.

[27] Ben Mildenhall, Pratul P. Srinivasan, Matthew Tancik, Jonathan T. Barron, Ravi Ramamoorthi, and Ren Ng. Nerf: Representing scenes as neural radiance fields for view synthesis. In *ECCV*. Springer, 2020.

[28] Thomas Müller, Alex Evans, Christoph Schied, and Alexander Keller. Instant-ngp: Instant neural graphics primitives with a multiresolution hash encoding. pages 1–15. ACM New York, NY, USA, 2022.

[29] Shu Naritomi and Keiji Yanai. Hungry networks: 3D mesh reconstruction of a dish and a plate from a single dish image for estimating food volume. In *ACM International Conference on Multimedia in Asia*, pages 1–7, 2021.

[30] Charles R. Qi, Hao Su, Kaichun Mo, and Leonidas J. Guibas. Pointnet: Deep learning on point sets for 3d classification and segmentation. In *CVPR*, 2017.

[31] Charles R. Qi, Li Yi, Hao Su, and Leonidas J. Guibas. Pointnet++: Deep hierarchical feature learning on point sets in a metric space. In *Advances in Neural Information Processing Systems (NeurIPS)*, 2017.

[32] Alexander Raistrick, Lahav Lipson, Zeyu Ma, Lingjie Mei, Mingzhe Wang, Yiming Zuo, Karhan Kayan, Hongyu Wen, Beining Han, Yihan Wang, et al. Infinite photorealistic worlds using procedural generation. In *CVPR*, pages 12630–12641, 2023.

[33] Nikhila Ravi, Valentin Gabeur, Yuan-Ting Hu, Ronghang Hu, Chaitanya Ryali, Tengyu Ma, Haitham Khedr, Roman Rädle, Chloe Rolland, Laura Gustafson, Eric Mintun, Junting Pan, Kalyan Vasudev Alwala, Nicolas Carion, Chao-Yuan Wu, Ross Girshick, Piotr Dollár, and Christoph Feichtenhofer. Sam 2: Segment anything in images and videos, 2024.

[34] Tianhe Ren, Qing Jiang, Shilong Liu, Zhaoyang Zeng, Wenlong Liu, Han Gao, Hongjie Huang, Zhengyu Ma, Xiaoke Jiang, Yihao Chen, Yuda Xiong, Hao Zhang, Feng Li, Peijun Tang, Kent Yu, and Lei Zhang. Grounding dino 1.5: Advance the "edge" of open-set object detection, 2024.

[35] Tianhe Ren, Shilong Liu, Ailing Zeng, Jing Lin, Kun-chang Li, He Cao, Jiayu Chen, Xinyu Huang, Yukang Chen, Feng Yan, Zhaoyang Zeng, Hao Zhang, Feng Li, Jie Yang, Hongyang Li, Qing Jiang, and Lei Zhang. Grounded sam: Assembling open-world models for diverse visual tasks, 2024.

[36] Johannes L. Schönberger and Jan-Michael Frahm. Structure-from-motion revisited. In *CVPR*, 2016.

[37] Wenjing Shao, Weiqing Min, Sujuan Hou, Mengjiang Luo, Tianhao Li, Yuanjie Zheng, and Shuqiang Jiang. Vision-based food nutrition estimation via RGB-D fusion network. *Food Chemistry*, 424:136309, 2023.

[38] Oriane Siméoni, Huy V. Vo, Maximilian Seitzer, Federico Baldassarre, Maxime Oquab, Cijo Jose, Vasil Khalidov, Marc Szafraniec, Seungeun Yi, Michaël Ramamonjisoa, Francisco Massa, Daniel Haziza, Luca Wehrstedt, Jianyuan Wang, Timothée Darcet, Théo Moutakanni, Leonel Sentana, Claire Roberts, Andrea Vedaldi, Jamie Tolan, John Brandt, Camille Couprise, Julien Mairal, Hervé Jégou, Patrick Latif, and Piotr Bojanowski. Dinov3, 2025.

[39] Maria Vasiloglou, Klazine Horst, Thomai Stathopoulou, Michael Jaeggi, Giulia Tedde, Ya Lu, and Stavroula Mougiakakou. The human factor in automated image-based nutrition apps: Analysis of common mistakes using the go-food lite app. *JMIR mHealth and uHealth*, 9:e24467, 2021.

[40] Gautham Vinod, Jiangpeng He, Zeman Shao, and Fengqing Zhu. Food portion estimation via 3d object scaling. In *CVPR*, pages 3741–3749, 2024.

[41] Jianyuan Wang, Minghao Chen, Nikita Karaev, Andrea Vedaldi, Christian Rupprecht, and David Novotny. Vggt: Visual geometry grounded transformer. In *CVPR*, pages 5294–5306, 2025.

[42] Yue Wang, Yongbin Sun, Ziwei Liu, Sanjay E. Sarma, Michael M. Bronstein, and Justin M. Solomon. Dynamic graph cnn for learning on point clouds. In *TOG*. ACM, 2019.

[43] Keyulu Xu, Weihua Hu, Jure Leskovec, and Stefanie Jegelka. How powerful are graph neural networks? In *ICLR*, 2019.

[44] Tao Yu, Zerong Zheng, Kaiwen Guo, Pengpeng Liu, Qionghai Dai, and Yebin Liu. Function4d: Real-time human volumetric capture from very sparse consumer rgbd sensors. In *CVPR*, 2021.

[45] Eleanor A Yudelman and Niall C Slowey. Coral extension rate analysis using computed axial tomography. *Coral Reefs*, 41(4):973–985, 2022.

[46] Yaofeng Yue, Wenyan Jia, John Fernstrom, Robert Sclabassi, Madely Fernstrom, Ning Yao, and Mingui Sun. Food volume estimation using a circular reference in image-based dietary studies. pages 1 – 2, 2010.

[47] Hengshuang Zhao, Li Jiang, Jiaya Jia, Philip H.S. Torr, and Vladlen Koltun. Point transformer. In *ICCV*, pages 16259–16268, 2021.

[48] Zheng Ziqiang, Xie Yaofeng, Liang Haixin, Yu Zhibin, and Sai-Kit Yeung. Coralvos: Dataset and benchmark for coral video segmentation. *arXiv preprint arXiv:2310.01946*, 2023.

Lightweight Neural Framework for Robust 3D Volume and Surface Estimation from Multi-View Images

Supplementary Material

A. Datasets Preparation Details

In this section, we describe the data generation and pre-processing pipelines used to create our training and evaluation datasets: Objaverse [3] (for pre-training), synthetic corals, human bodies (THuman 2.1 [18]), and real food items (CVPR MetaFood [2]).

A.1. Objaverse

For Objaverse, we start from the textured Objaverse meshes converted to OBJ format, retaining both a raw textured version for rendering and a watertight counterpart for reliable geometry measurements. The dataset consists of $\approx 32,000$ assets. For each object, we load the mesh and translate it to the origin. Ground-truth volume and surface area are computed from the watertight mesh using Trimesh, as detailed in the main paper. Multi-view RGB images are rendered off-screen in PyVista on a black background at $\approx 682 \times 512$ resolution, sampling 40 camera poses per object with azimuth uniformly in $[0^\circ, 360^\circ]$, elevation restricted away from the poles ($|\text{elev}| < 84^\circ$), distance in $(3.0\text{--}3.7) \times$ the object extent (with a mild bias toward closer views), and focal-point jitter $\pm 0.03 \times$ the extent. The field of view is randomized in $24^\circ\text{--}28^\circ$ and the up-vector is fixed to $[0, 0, 1]$. Lighting uses 25–35 scene lights with evenly spaced azimuth, random elevations in $[-80^\circ, 80^\circ]$, and intensity 0.13–0.16, while PBR shading parameters are lightly randomized (ambient 0.15–0.30, diffuse 0.5–0.7, specular 0.15–0.3, specular power 5–10). For each rendered view, we save the RGB image and the corresponding camera parameters (position, quaternion, distance, angles, jitter, and FoV).

A.2. Synthetic and Real Corals

As mentioned in the main paper, using Infinigen [10], we generated a synthetic coral dataset, that contains textured meshes of more than 4000 different corals, with substantial variability in terms of represented species and size. From this dataset, we render multi-view RGB images using PyVista. Each rendered view has a resolution of 1024×768 pixels with a field of view ranging from 22° to 40° . We apply a slight random camera jitter to avoid pointing exactly at the object center; backgrounds are removed at render time, producing black-padded, centered images with a small random translation. Lighting uses 32 scene lights evenly spaced over 360° azimuth, elevations $10^\circ\text{--}80^\circ$, intensity 0.18; shading is PBR-style with ambient 0.2, diffuse 0.9, specular 0.4, and full opacity. This setup ensures var-

ied lighting and viewpoints while maintaining object focus. Note that this process is performed before applying **ManifoldPlus** [5] to produce watertight (textureless) geometry. The watertight geometry is solely used for ground-truth volume and surface area computation.

For real corals, we physically suspended each specimen on a thin cable and captured images all around it, collecting over 100 RGB views per coral (see Fig. S5 for real and synthetic corals utilized in our experiments). During fine-tuning, we vary the number of input images from 1 to 40 by randomly sampling subsets from these 100+ views for each coral.

A.3. THuman 2.1

The Thuman [18] is a dataset of high-quality human scans captured using a dense DSLR rig. Each scan contains a 3D model with its corresponding texture map. Similarly to the synthetic corals dataset, we adopted a strategy of rendering images with black backgrounds and random view sampling. We render images in PyVista following the Objaverse protocol. We also adopt the same lighting parameters. The PBR shading parameters are as follows: (ambient 0.22–0.33, diffuse 0.5–0.7, specular 0.16–0.3, specular power 5–10, and full opacity).

A.4. Food (CVPR MetaFood)

For the CVPR MetaFood dataset [2], we focused on real-world images and applied segmentation to isolate food items, incorporating manual quality assessment to address potential inconsistencies.

Specifically, we used Grounded-SAM2 (combining Grounding DINO [14] and SAM 2 for open-world, promptable segmentation) [6, 8, 9, 11–13], by prompting the model with the food class name. Only masks that accurately segmented the food items were retained after manual review, ensuring the final inputs aligned with ground-truth assets. As discussed in the Methods section in the main paper and depicted in Figure S1, some classes in the MetaFood dataset exhibit ambiguities between the annotated volume (container + food) and the segmented region (food only). Such cases motivated the manual quality assessment step, where we filtered the masks to ensure that the supervision is consistent with the ground-truth assets.

B. Network Architecture and Training Details

Overall design. Our regressor operates on precomputed 3D point clouds with per-point features and DINO descrip-

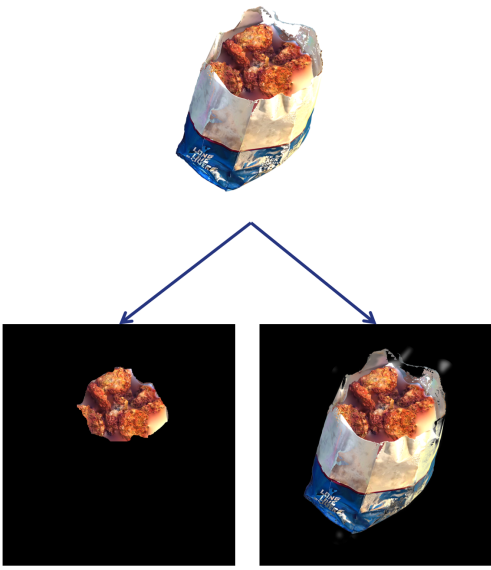


Figure S1. Example of segmentation inconsistencies in the MetaFood dataset. While some masks correctly isolate the full object (right), others segment only the food portion inside a container (left). This ambiguity arises because, in certain classes, the ground-truth volume refers to both the container and its contents, while the mask includes only the food. Manual quality assurance (QA) was therefore required to ensure consistency across samples. Representative segmentation examples were generated using Grounded-SAM2.

tors. For each object, we use a point-wise feature tensor of dimension 4 (3D coordinates plus one confidence scalar attribute) and a per-point DINO feature of dimension $d_{\text{DINO}} = 384$. The network has two main branches: a 3D branch (MapAnything [7]) and a 2D branch (DINO-feature encoder), followed by a DGCNN [16] as output of the 3D branch, fusion MLP and a small regression head that predicts the target scalar (volume or surface area) and its corresponding confidence. We use MapAnything as our default 3D reconstructor since it is computationally faster in our setup and remains stable in GPU memory when scaling to many input views, whereas VGGT often triggers out-of-memory errors in these regimes.

DGCNN-style point cloud branch. The point cloud encoder follows a DGCNN pattern built on a k -nearest neighbor graph with $k = 30$. Starting from input features of dimension 4, we construct edge features via `get_graph_feature`, which concatenates central and neighbor differences. These edge features are processed by five successive convolutional layers with 64, 64, 128, 256, and 256 channels, respectively. Each convolutional block consists of a 1×1 convolution, `InstanceNorm2d`, and a LeakyReLU non-linearity with negative slope 0.2, followed

by a max aggregation over neighbors.

We then concatenate the intermediate feature maps from selected stages (x_2, x_4, x_5), obtaining a 576-dimensional per-point representation. A global adaptive max-pooling over points yields a single 576-dimensional descriptor for the entire cloud. This descriptor is passed through three fully connected layers of sizes $576 \rightarrow 512$, $512 \rightarrow 256$, and $256 \rightarrow 128$, each followed by `LayerNorm`, LeakyReLU (0.2), and dropout with rate of 0.3. The result is a compact 128-dimensional global embedding of the 3D geometry.

DINO feature branch. In parallel, we process the per-image DINO features through a two-layer MLP with hidden size 256 and output size 128. Each layer is followed by `LayerNorm`, LeakyReLU (0.2), and dropout (0.3). This yields a 128-dimensional feature for each image. We aggregate these features across different views using both max-pooling and mean-pooling and concatenate the two pooled vectors, resulting in a 256-dimensional global DINO descriptor.

Fusion and regression head. We fuse the two branches (2D and 3D branches) by concatenating the 128-dimensional latent code output by the 3D branch with the 256-dimensional DINO embedding into a single 384-dimensional vector. This fused representation passes through a two-layer MLP with sizes $384 \rightarrow 256$ and $256 \rightarrow 128$, each with `LayerNorm`, LeakyReLU (0.2), and dropout (0.3). The final regression head is a single linear layer mapping the 128-dimensional fused feature to 2 outputs: the predicted volume or surface area μ_{real} and a log-variance term $\log \sigma^2$. To enforce positivity of the predicted geometric attribute, we apply a `softplus` activation to the first output; the second output is used directly as the log-variance parameter.

Loss function and uncertainty. We train the model with a custom loss that combines a Gaussian negative log-likelihood (NLL) term with a deterministic error term. The NLL is computed jointly in the original scale and in log-space, with a fixed weighting (0.3 for the real-space term and 0.7 for the log-space term). To balance with the deterministic component (the relative error term) we use a coefficient $\gamma = 0.2$. Additionally, we optionally include a median MAPE regularizer with a small weight α , which encourages the model to control large relative errors. The log-variance output describes uncertainty and is passed through `softplus` to obtain a positive variance before computing the NLL.

Optimization and learning rate schedule. We optimize all models with AdamW using an initial learning rate of 1.6×10^{-4} and a weight decay of 10^{-4} .

We employ a cosine annealing learning-rate schedule (CosineAnnealingLR) with $T_{\max} = 60$ epochs and a minimum learning rate of 2×10^{-6} . Training is run for up to 650 epochs; early stopping was applied.

Implementation details. We train with a batch size of 1 (one object per batch), which is sufficient given the large number of points per cloud. We use mixed-precision training via `torch.cuda.amp` (automatic casting and gradient scaling) to reduce memory usage and accelerate training. Random seeds for PyTorch and NumPy are fixed to 42 (including dataloader workers) to ensure reproducibility. During training and evaluation, we track MAE, RMSE, and MAPE on both training and validation sets and export detailed metrics and per-sample predictions for downstream analysis.

Additional data augmentation details. Beyond the description in the main paper, each point cloud undergoes a deterministic preprocessing step before augmentations are applied. We first recenter the 3D coordinates by subtracting their centroid and rescale them by the maximum axis-aligned extent so that all objects fit inside a unit bounding box. If a point cloud contains more than a fixed budget of points ($N_{\max} = 50,000$), we randomly subsample N_{\max} points without replacement; samples with fewer than a minimum number of points (e.g., $N_{\min} = 20,000$) are discarded during dataset construction.

When Gaussian jitter is enabled, it is implemented as isotropic noise $\varepsilon \sim \mathcal{N}(0, \sigma^2 I_3)$ on the normalized coordinates with a small standard deviation $\sigma = 0.001$. All augmentations (rotations, reflections, jitter and subsampling) operate strictly on the (x, y, z) coordinates, leaving features and DINO descriptors unchanged.

Environment. The models were run on a single Nvidia A100 GPU on a Linux cluster using Python and PyTorch. Key tools include libraries like PyVista/Trimesh for ground-truth computation and rendering, as well as repositories of the pre-trained models utilized for the framework and benchmarks (Trellis [17], MapAnything [7], VGTT [15], 2DGS [4], Agisoft). For training, we used a 80/20 train/validation split.

C. Additional Results

Table S1, complements the THuman ablation results in the main paper, showing the model’s performance with varying numbers of samples on the synthetic corals and MetaFood datasets.

Table S2 reports all the results for the CVPR MetaFood Challenge, including our framework, ININ and VolETA [1, 2]. The table consists of three different types of scenes:

Table S1. MetaFood and synthetic corals: MAPE (mean, median) vs. number of samples per object (lower is better).

# Samples	MetaFood				Synthetic corals			
	Vol. Mean	MAPE ↓ Med.	Surf. Mean	MAPE ↓ Med.	Vol. Mean	MAPE ↓ Med.	Surf. Mean	MAPE ↓ Med.
1	17.22	10.13	19.59	11.09	16.49	12.94	10.91	8.18
2	18.05	10.32	20.18	11.95	13.20	8.61	11.23	9.61
4	13.38	8.13	23.06	12.92	11.27	9.01	9.03	7.31
8	13.46	8.96	20.15	11.61	10.38	7.47	7.92	6.68
16	8.50	5.88	17.45	10.25	10.15	7.31	7.57	5.50
32	7.69	5.50	17.09	9.88	9.61	6.94	7.32	5.78
64	8.05	6.31	17.97	10.75	9.16	6.96	6.96	5.01
100+	7.46	5.39	19.40	10.38	8.96	6.41	6.78	4.86

Table S2. CVPR Metafood Challenge: Per-scene error percentage (MAPE = $|\hat{v} - v|/v \cdot 100$). Best (lowest) per row in **bold**. Dashes (–) = not reported.

Idx	Ours (%)	ININ (%)	VolETA (%)
1	8.80	15.52	3.97
2	4.94	14.59	22.64
3	46.94	34.62	11.69
4	19.65	17.76	5.46
5	8.61	0.84	0.81
6	4.08	9.44	6.07
7	30.55	11.86	1.13
8	28.63	4.67	7.79
9	2.03	0.45	3.72
10	1.16	1.86	5.72
11	46.49	0.96	5.61
12	0.00	–	–
13	3.33	8.57	18.07
14	21.11	12.22	9.22
15	8.58	–	–
16	6.16	32.77	37.77
17	1.38	0.37	23.56
18	18.77	34.01	23.42
19	25.23	8.64	1.57
20	8.01	20.03	9.29

simple (first 8 scenes, 200 images) medium (scene between 9 and 15, 30 images) and hard (between 16 and 20, single view).

Table S3 compares our framework on synthetic corals against an MVS-based baseline using Agisoft and the Trellis pipeline. We evaluate three input regimes: single view, 5 views, and 30 views on a subset of 15 synthetic coral assets drawn from the main paper test set. For the single-view setting, we render 35 independent views per asset and run inference on each view separately; we then aggregate the resulting volume and surface predictions across all views and assets to report mean and median MAPE.

For the case of 5 and 30 images, we first use Agisoft to reconstruct a mesh from the multi-view images, then we postprocess the mesh to remove some edge vertices that represent the black background and convert it to a watertight mesh. Finally, we use Trimesh to compute the volume and surface as described in the main paper. This shows that our learned regressor can extract reliable 3D cues even in the

Table S3. Synthetic corals: mean and median MAPE for volume and surface (lower is better) for a single image, 5 and 30 input views. The baseline is Agisoft; “–” indicates configurations not possible to evaluate for that method.

Dataset	# Views	Stat.	Ours		Trellis		Agisoft	
			Vol	Surf	Vol	Surf	Vol	Surf
			Mean	22.08	13.71	87.00	64.65	–
Corals	5	Single image	Median	18.21	10.24	85.41	67.58	–
		Mean	23.36	12.59	–	–	126.85	47.90
		Median	15.97	6.28	–	–	69.13	47.41
	30	Mean	19.33	10.28	–	–	93.12	41.49
		Median	15.57	7.53	–	–	63.70	46.41

most challenging single-view setting, where Agisoft cannot be applied. When more views are available, our performance remains strong or improves slightly. Furthermore, it vastly outperforms Trellis on a single image which also fails to accurately regressing volume and surface area from the reconstructed meshes. Overall, our approach is both more data efficient, performing well even from a single image, and more robust as the number of views increases; while Agisoft and Trellis either cannot be evaluated in some settings or remain significantly less accurate (see Fig. S6).

Uncertainty. Figures S2, S4, S3 report the distribution of predicted uncertainties for different numbers of input views and for both volume and surface. Uncertainty values are normalized to [0,1] over the entire dataset. Under this normalization, values close to 0 indicate low predictive uncertainty, whereas values close to 1 indicate high predictive uncertainty. Across all datasets, the histograms are usually strongly concentrated and show a gradual shift of the mean and median toward lower values as the number of views increases, indicating higher confidence and lower uncertainty with more observations. The effect is more pronounced when going from 1 to 16-32 views, after which the returns slowly diminish.

References

- [1] Ahmad AlMughrabi, Umair Haroon, Ricardo Marques, and Petia Radeva. Voleta: One-and few-shot food volume estimation. *arXiv preprint arXiv:2407.01717*, 2024.
- [2] Yuhao Chen, Jiangpeng He, Gautham Vinod, Siddeshwar Raghavan, Chris Czarnecki, Jinge Ma, Talha Ibn Mahmud, Bruce Coburn, Dayou Mao, Saejith Nair, et al. Metafood3d: 3d food dataset with nutrition values. *arXiv preprint arXiv:2409.01966*, 2024.
- [3] Matt Deitke, Dustin Schwenk, Jordi Salvador, Luca Weihs, Oscar Michel, Eli VanderBilt, Ludwig Schmidt, Kiana Ehsani, Aniruddha Kembhavi, and Ali Farhadi. Objaverse: A universe of annotated 3d objects. In *Proceedings of the IEEE/CVF conference on computer vision and pattern recognition*, pages 13142–13153, 2023.
- [4] Binbin Huang, Zehao Yu, Anpei Chen, Andreas Geiger, and Shenghua Gao. 2D gaussian splatting for geometrically accurate radiance fields. In *ACM SIGGRAPH 2024 conference papers*, pages 1–11, 2024.
- [5] Jingwei Huang, Yichao Zhou, and Leonidas Guibas. Manifoldplus: A robust and scalable watertight manifold surface generation method for triangle soups. *arXiv preprint arXiv:2005.11621*, 2020.
- [6] Qing Jiang, Feng Li, Zhaoyang Zeng, Tianhe Ren, Shilong Liu, and Lei Zhang. T-rex2: Towards generic object detection via text-visual prompt synergy, 2024.
- [7] Nikhil Keetha, Norman Müller, Johannes Schönberger, Lorenzo Porzi, Yuchen Zhang, Tobias Fischer, Arno Knapitsch, Duncan Zauss, Ethan Weber, Nelson Antunes, Jonathon Luiten, Manuel Lopez-Antequera, Samuel Rota Bulò, Christian Richardt, Deva Ramanan, Sebastian Scherer, and Peter Kortschieder. Mapanything: Universal feed-forward metric 3d reconstruction, 2025.
- [8] Alexander Kirillov, Eric Mintun, Nikhila Ravi, Hanzi Mao, Chloe Rolland, Laura Gustafson, Tete Xiao, Spencer Whitehead, Alexander C. Berg, Wan-Yen Lo, Piotr Dollár, and Ross Girshick. Segment anything. *arXiv:2304.02643*, 2023.
- [9] Shilong Liu, Zhaoyang Zeng, Tianhe Ren, Feng Li, Hao Zhang, Jie Yang, Chunyuan Li, Jianwei Yang, Hang Su, Jun Zhu, et al. Grounding dino: Marrying dino with grounded pre-training for open-set object detection. *arXiv preprint arXiv:2303.05499*, 2023.
- [10] Alexander Raistrick, Lahav Lipson, Zeyu Ma, Lingjie Mei, Mingzhe Wang, Yiming Zuo, Karhan Kayan, Hongyu Wen, Beining Han, Yihan Wang, et al. Infinite photorealistic worlds using procedural generation. In *CVPR*, pages 12630–12641, 2023.
- [11] Nikhila Ravi, Valentin Gabeur, Yuan-Ting Hu, Ronghang Hu, Chaitanya Ryali, Tengyu Ma, Haitham Khedr, Roman Rädle, Chloe Rolland, Laura Gustafson, Eric Mintun, Junting Pan, Kalyan Vasudev Alwala, Nicolas Carion, Chao-Yuan Wu, Ross Girshick, Piotr Dollár, and Christoph Feichtenhofer. Sam 2: Segment anything in images and videos, 2024.
- [12] Tianhe Ren, Qing Jiang, Shilong Liu, Zhaoyang Zeng, Wenlong Liu, Han Gao, Hongjie Huang, Zhengyu Ma, Xiaoke Jiang, Yihao Chen, Yuda Xiong, Hao Zhang, Feng Li, Peijun Tang, Kent Yu, and Lei Zhang. Grounding dino 1.5: Advance the “edge” of open-set object detection, 2024.
- [13] Tianhe Ren, Shilong Liu, Ailing Zeng, Jing Lin, Kun-chang Li, He Cao, Jiayu Chen, Xinyu Huang, Yukang Chen, Feng Yan, Zhaoyang Zeng, Hao Zhang, Feng Li, Jie Yang,

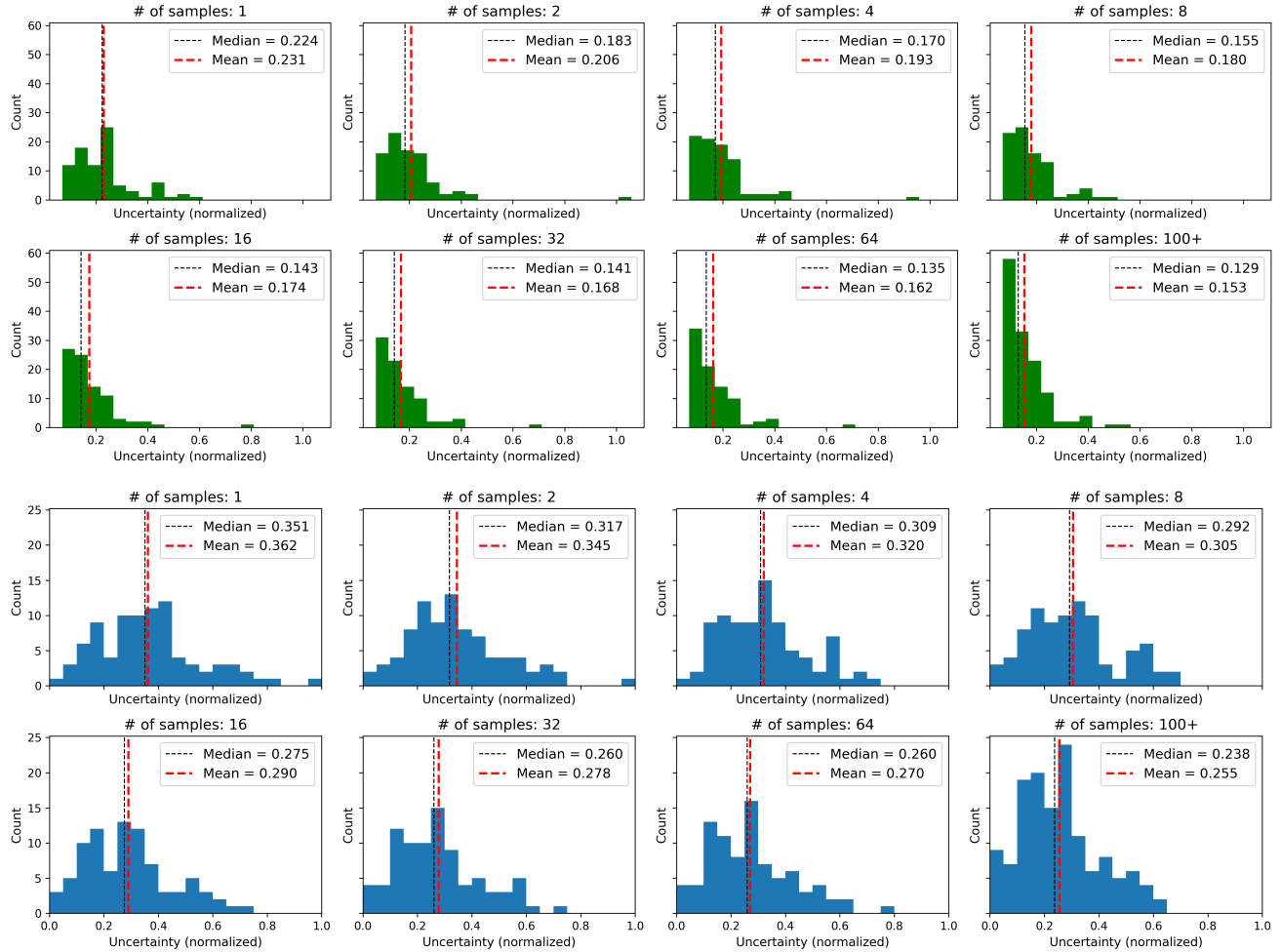


Figure S2. **MetaFood.** Histograms of the predicted normalized uncertainty for different numbers of input views: volume (top) and surface (bottom).

Hongyang Li, Qing Jiang, and Lei Zhang. Grounded sam: Assembling open-world models for diverse visual tasks, 2024.

[14] Oriane Siméoni, Huy V. Vo, Maximilian Seitzer, Federico Baldassarre, Maxime Oquab, Cijo Jose, Vasil Khalidov, Marc Szafraniec, Seungeun Yi, Michaël Ramamonjisoa, Francisco Massa, Daniel Haziza, Luca Wehrstedt, Jianyuan Wang, Timothée Darcet, Théo Moutakanni, Leonel Sentana, Claire Roberts, Andrea Vedaldi, Jamie Tolan, John Brandt, Camille Couprie, Julien Mairal, Hervé Jégou, Patrick Lat batut, and Piotr Bojanowski. Dinov3, 2025.

[15] Jianyuan Wang, Minghao Chen, Nikita Karaev, Andrea Vedaldi, Christian Rupprecht, and David Novotny. Vggt: Visual geometry grounded transformer. In *CVPR*, pages 5294–5306, 2025.

[16] Yue Wang, Yongbin Sun, Ziwei Liu, Sanjay E. Sarma, Michael M. Bronstein, and Justin M. Solomon. Dynamic graph cnn for learning on point clouds. In *TOG*. ACM, 2019.

[17] Jianfeng Xiang, Zelong Lv, Sicheng Xu, Yu Deng, Ruicheng Wang, Bowen Zhang, Dong Chen, Xin Tong, and Jiaolong Yang. Trellis: Structured 3d latents for scalable and versatile 3d generation. In *CVPR*, pages 21469–21480, 2025.

[18] Tao Yu, Zerong Zheng, Kaiwen Guo, Pengpeng Liu, Qionghai Dai, and Yebin Liu. Function4d: Real-time human volumetric capture from very sparse consumer rgbd sensors. In *CVPR*, 2021.

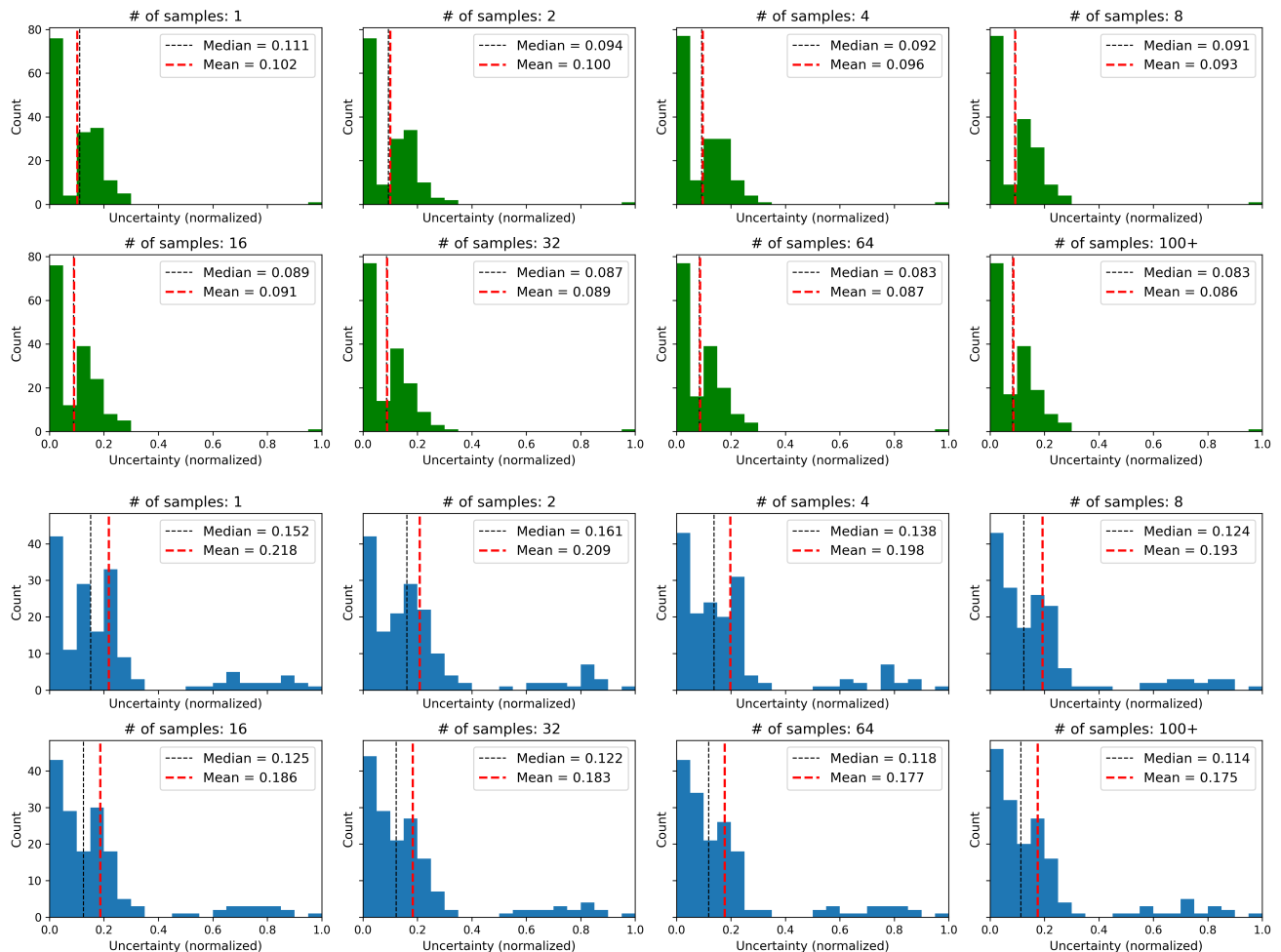


Figure S3. **Synthetic corals.** Histograms of the predicted normalized uncertainty for different numbers of input views: volume (top) and surface (bottom).

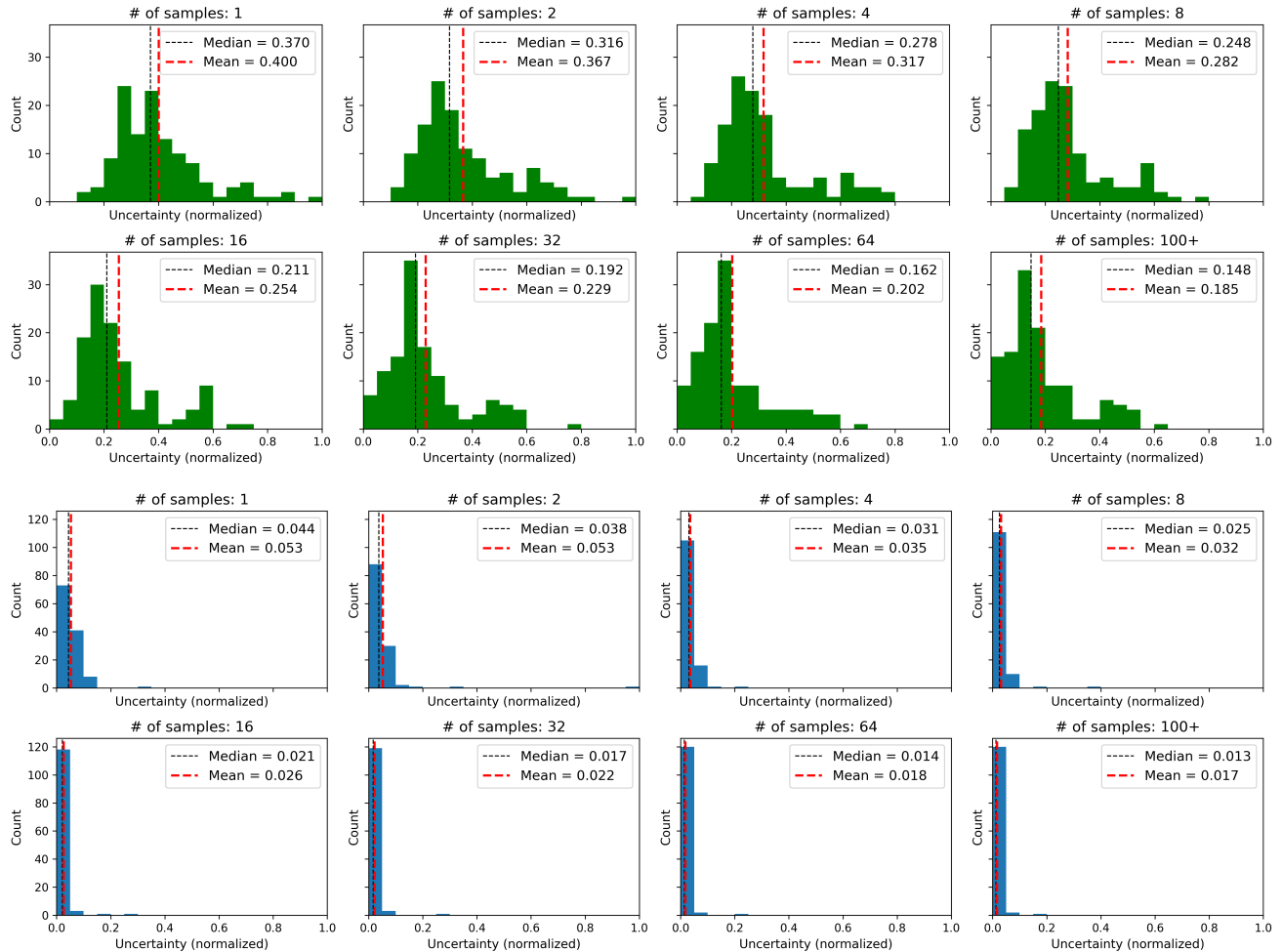


Figure S4. **THuman**. Histograms of the predicted normalized uncertainty for different numbers of input views: volume (top) and surface (bottom).

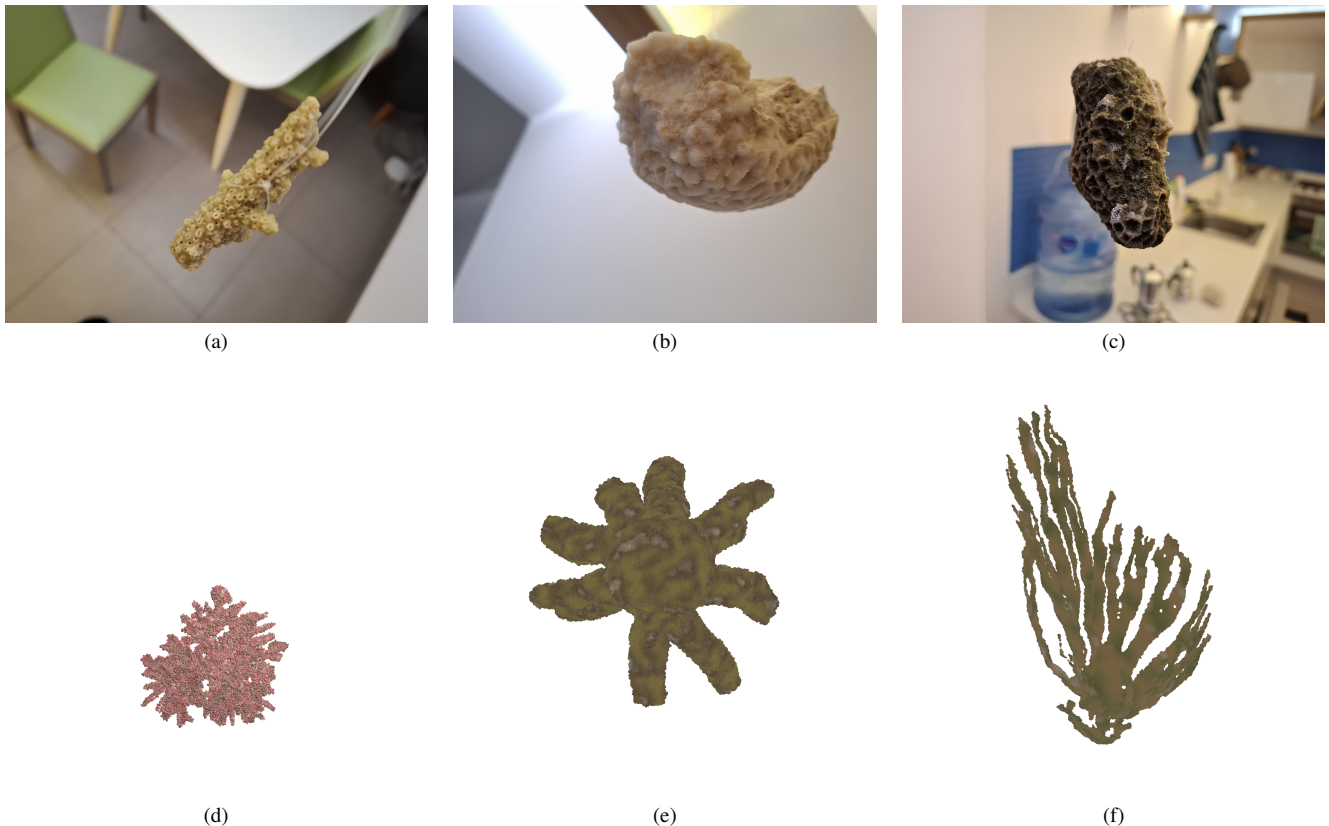


Figure S5. Images of collected real corals (first row), and snapshots of synthetic corals (second row).



Figure S6. Left: ground-truth image. Right: Agisoft reconstruction using 30 images, which fails to recover the correct geometry and appearance in most cases.